

SCIENTIFIC REPORTS

OPEN

A comparative study of ZnAl_2O_4 nanoparticles synthesized from different aluminum salts for use as fluorescence materials

Received: 21 January 2015

Accepted: 08 July 2015

Published: 04 August 2015

Shi-Fa Wang^{1,2}, Guang-Zhuang Sun^{1,2}, Lei-Ming Fang², Li Lei³, Xia Xiang¹ & Xiao-Tao Zu¹

Three ZnAl_2O_4 samples were prepared via a modified polyacrylamide gel method using a citric acid solution with different aluminum salt starting materials, including $\text{AlCl}_3 \cdot 6\text{H}_2\text{O}$, $\text{Al}_2(\text{SO}_4)_3 \cdot 18\text{H}_2\text{O}$, and $\text{Al}(\text{NO}_3)_3 \cdot 9\text{H}_2\text{O}$ under identical conditions. The influence of different aluminum salts on the morphologies, phase purity, and optical and fluorescence properties of the as-prepared ZnAl_2O_4 nanoparticles were studied. The experimental results demonstrate that the phase purity, particle size, morphology, and optical and fluorescence properties of ZnAl_2O_4 nanoparticles can be manipulated by the use of different aluminum salts as starting materials. The energy bandgap (Eg) values of ZnAl_2O_4 nanoparticles increase with a decrease in particle size. The fluorescence spectra show that a major blue emission band around 400 nm and two weaker side bands located at 410 and 445 nm are observed when the excitation wavelength is 325 nm. The ZnAl_2O_4 nanoparticles prepared from $\text{Al}(\text{NO}_3)_3 \cdot 9\text{H}_2\text{O}$ exhibit the largest emission intensity among the three ZnAl_2O_4 samples, followed in turn by the ZnAl_2O_4 nanoparticles prepared from $\text{Al}_2(\text{SO}_4)_3 \cdot 18\text{H}_2\text{O}$ and $\text{AlCl}_3 \cdot 6\text{H}_2\text{O}$. These differences are attributed to combinational changes in Eg and the defect types of the ZnAl_2O_4 nanoparticles.

Spinel ZnAl_2O_4 is known to have a wide energy bandgap (Eg), high mechanical resistance, high fluorescence efficiency, high chemical and thermal stability, high photocatalytic activity, and low surface acidity, all of which make it a suitable material for a wide range of applications, including use in photoelectronic devices, catalysts, electroluminescence displays, stress imaging devices, optical coatings, and highly efficient phosphors^{1–3}. Based on the above mentioned applications, various morphologies of spinel ZnAl_2O_4 have been prepared, including one-dimensional microfibers, porous structures, nanoparticles, nanorods, nanotubes, and so on^{4–8}. It has been noted that the optical properties of these materials are strongly dependent on their morphologies and preparation methods. In particular, ZnAl_2O_4 nanostructures are expected to exhibit enhanced optical and fluorescence properties usually absent in bulk ZnAl_2O_4 . Therefore, the preparation and study of the optical and fluorescence properties of ZnAl_2O_4 nanostructure powder is of great interest.

Spinel ZnAl_2O_4 semiconductors have been synthesized using a variety of different methods, such as the solid-state reaction method^{9,10}, a self-generated template pathway⁹, the combustion synthesis route¹¹, the sol-gel method¹², a co-precipitation approach⁶, the polymeric precursor method¹³, the citrate precursor method⁴, a hydrothermal process⁷, a solvothermal approach¹⁴, and the microwave-hydrothermal route¹⁵. The particle size of ZnAl_2O_4 has a large effect on its optical and fluorescence properties. Generally,

¹School of Physical Electronics and Institute of Fundamental and Frontier Sciences, University of Electronic Science and Technology of China, Sichuan, Chengdu, 610054, China. ²Institute of Nuclear Physics and Chemistry, China Academy of Engineering Physics, Sichuan, Mianyang, 621900, China. ³Institute of Atomic and Molecular Physics, Sichuan University, 610065, Chengdu, China. Correspondence and requests for materials should be addressed to X.T.Z. (email: xtzu@uestc.edu.cn)

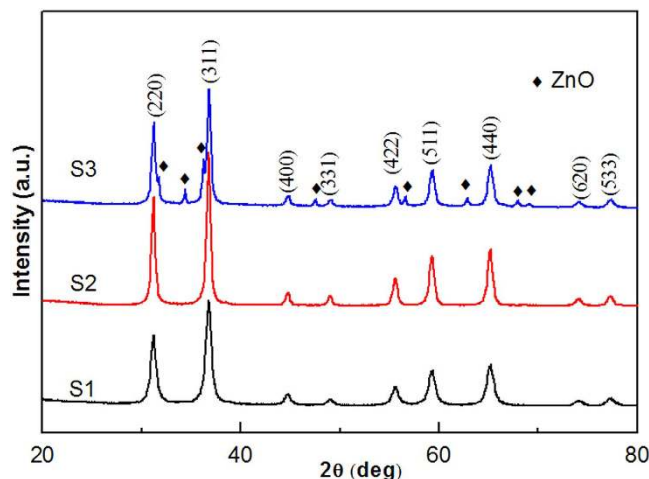


Figure 1. XRD patterns of ZnAl_2O_4 nanoparticles prepared from (S1) $\text{Al}_2(\text{SO}_4)_3 \cdot 18\text{H}_2\text{O}$, (S2) $\text{AlCl}_3 \cdot 6\text{H}_2\text{O}$, and (S3) $\text{Al}(\text{NO}_3)_3 \cdot 9\text{H}_2\text{O}$ and sintered at 600°C .

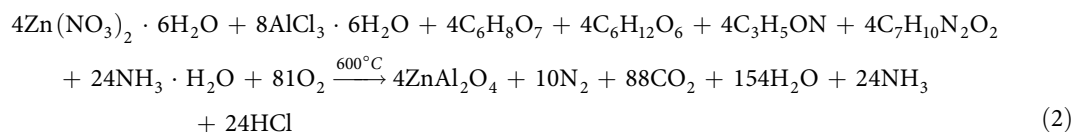
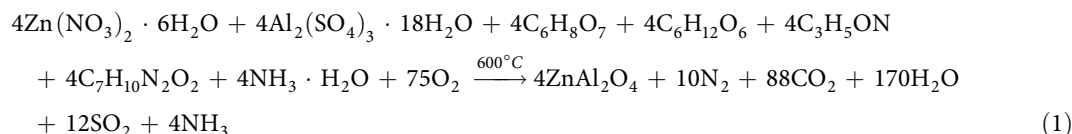
smaller particles have a relatively larger specific surface area, and therefore have a larger amount of dangling and unsaturated bonds on the particle surface. This in turn affects the defect levels and fluorescence properties of the powder¹⁶. However, the main disadvantage of preparing spinel ZnAl_2O_4 by the traditional synthesis routes, such as the co-precipitation approach, the solid-state reaction method, and others, is the large particle size of the product.

The polyacrylamide gel route is a very good sol-gel method for the preparation of superfine nanoparticles¹⁷. Appropriate selection of a chelating agent, monomer systems, initiator, pH value, and sintering temperature can significantly improve the quality of the prepared nanoparticles¹⁷. In addition, different aluminum salts, i.e. different anionic species in the precursor solutions, can greatly influence the morphology, phase purity, and optical and fluorescence properties of the ZnAl_2O_4 . However, most previously reported studies have only used a single aluminum salt as a starting material and have not investigated the influences of different aluminum salts on the morphology, structure, and optical and fluorescence properties of the obtained ZnAl_2O_4 .

In this study, three different aluminum salts are used as starting materials to synthesize three ZnAl_2O_4 gels via a polyacrylamide gel route, specifically aqueous solutions of citric acid with $\text{Al}_2(\text{SO}_4)_3 \cdot 18\text{H}_2\text{O}$, $\text{AlCl}_3 \cdot 6\text{H}_2\text{O}$, or $\text{Al}(\text{NO}_3)_3 \cdot 9\text{H}_2\text{O}$ were used under identical conditions. In order to obtain superfine nanoparticles, *N,N'*-methylene-bisacrylamide was used as a cross-linking agent, and glucose was used to prevent gel collapse. After sintering these xerogels, three ZnAl_2O_4 nanostructure samples were obtained. Their phase purity, morphologies, and optical and fluorescence properties were then characterized and compared. The objective of the present work is to investigate the influence of different aluminum salt starting materials on the resulting ZnAl_2O_4 nanostructures and on their optical and fluorescence properties.

Results

The obtained ZnAl_2O_4 xerogels decomposed into products after being sintered at 600°C for 5 h in air. Figure 1 shows the XRD patterns of ZnAl_2O_4 nanoparticles prepared from (S1) $\text{Al}_2(\text{SO}_4)_3 \cdot 18\text{H}_2\text{O}$, (S2) $\text{AlCl}_3 \cdot 6\text{H}_2\text{O}$, and (S3) $\text{Al}(\text{NO}_3)_3 \cdot 9\text{H}_2\text{O}$. It can be seen that samples S1 and S2 have crystallized in a single phase with a spinel structure and with space group $O7h$, but sample S3 contains small amounts of ZnO (JCPDS card No. 36–1451) impurities in addition to the major phase of spinel ZnAl_2O_4 structure (JCPDS card No. 05–0669). According to the literature^{2,18}, the relevant reactions can be described by the following equations:



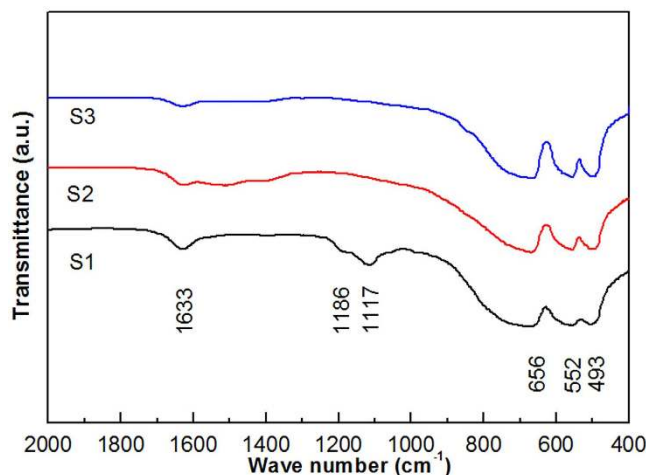
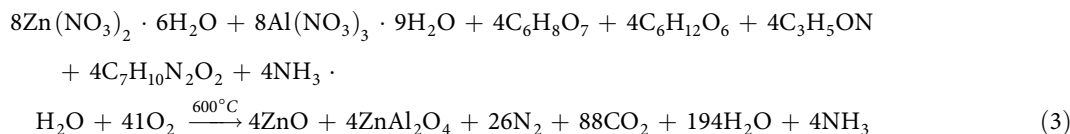


Figure 2. FT-IR spectrum of ZnAl_2O_4 nanoparticles prepared from (S1) $\text{Al}_2(\text{SO}_4)_3 \cdot 18\text{H}_2\text{O}$, (S2) $\text{AlCl}_3 \cdot 6\text{H}_2\text{O}$, and (S3) $\text{Al}(\text{NO}_3)_3 \cdot 9\text{H}_2\text{O}$ and sintered at 600°C .



For samples S1 and S2, the observed diffraction peaks at 2θ are 31.22, 36.77, 44.69, 48.98, 55.52, 59.27, 65.06, 73.97, and 77.12 and can be ascribed, respectively, to the (220), (311), (400), (331), (422), (511), (440), (620), and (533) planes of ZnAl_2O_4 . The mean grain size of samples S1, S2, and S3 were quantitatively evaluated based on the line broadening of the (220), (311), (511), and (440) peaks using the Scherrer formula, to be 13, 16, and 24 nm, respectively. XRD results indicate that the choice of the aluminum salts also has an influence on the phase purity of the final product. A possible reason for the formation of impurity phases when using citric acid as a chelating agent is that citric acid has a relatively weak coordinating capacity toward the metal ion of $\text{Al}(\text{NO}_3)_3 \cdot 9\text{H}_2\text{O}$, and hence the formed metal complexonate is not expected to be highly stable.

Fourier transform infrared (FT-IR) spectra of the ZnAl_2O_4 nanoparticles prepared from (S1) $\text{Al}_2(\text{SO}_4)_3 \cdot 18\text{H}_2\text{O}$, (S2) $\text{AlCl}_3 \cdot 6\text{H}_2\text{O}$, and (S3) $\text{Al}(\text{NO}_3)_3 \cdot 9\text{H}_2\text{O}$ are shown in Fig. 2. The FT-IR spectra show a series of absorption peaks in the range of $400\text{--}2000\text{ cm}^{-1}$. According to the specific frequencies of the absorption peaks, the functional groups existing in the samples can be deduced. Peaks at 1633, 656, 552, and 493 cm^{-1} are present in all samples, and are assigned to the H-O-H bending vibration of adsorbed water¹⁹, Al-O symmetric stretching vibration (ν_1)^{19–22}, Al-O symmetric bending vibration (ν_2)^{19–22}, and Al-O asymmetric stretching vibration (ν_3)^{21,22}, respectively. For sample S2, the peaks located at 1186 and 1117 cm^{-1} are attributed to the S=O asymmetric stretching vibration²³ and the S-O symmetric stretching vibration^{23,24}, respectively.

Figure 3 shows the TG/DTA curves of the ZnAl_2O_4 xerogels obtained from (S1) $\text{Al}_2(\text{SO}_4)_3 \cdot 18\text{H}_2\text{O}$, (S2) $\text{AlCl}_3 \cdot 6\text{H}_2\text{O}$, and (S3) $\text{Al}(\text{NO}_3)_3 \cdot 9\text{H}_2\text{O}$. There are four weight loss stages observed for each sample. The first weight loss stage is seen at a low temperature range (before 200°C) and corresponds to the evaporation of surface water in the ZnAl_2O_4 xerogel precursors^{25,26}. The second weight loss stage (around $200\text{--}250^\circ\text{C}$) is due to the evaporation of structural water^{25,26}. The third weight loss stage (between $250\text{--}400^\circ\text{C}$) is due to the decomposition of small molecular organic compounds. The largest and final weight loss stage (around $400\text{--}620^\circ\text{C}$) is due to decomposition of complexes, glucose, and the polyacrylamide side-chain, as well as combustion of the polyacrylamide backbone and other residues^{27,28}. The total weight loss measured for the ZnAl_2O_4 xerogel precursors were 97.31% for (S1) $\text{Al}_2(\text{SO}_4)_3 \cdot 18\text{H}_2\text{O}$, 95.201% for (S2) $\text{AlCl}_3 \cdot 6\text{H}_2\text{O}$, and 98.234% for (S3) $\text{Al}(\text{NO}_3)_3 \cdot 9\text{H}_2\text{O}$. In Fig. 3 (S1), the main endothermic peak appeared at around 535°C and corresponds to the thermal decomposition of the complexes, polyacrylamide backbone, and other residues originating from $\text{Al}_2(\text{SO}_4)_3 \cdot 18\text{H}_2\text{O}$. Meanwhile, the main endothermic peaks appeared at 557°C (Fig. 3(S2)) for the ZnAl_2O_4 xerogel precursor obtained from $\text{AlCl}_3 \cdot 6\text{H}_2\text{O}$, and at 528°C (Fig. 3(S3)) for (S3) $\text{Al}(\text{NO}_3)_3 \cdot 9\text{H}_2\text{O}$. The slightly different decomposition temperatures of the three ZnAl_2O_4 xerogels may be related to differences in the microstructures caused by the presence of different anionic species (Cl^- , SO_4^{2-} , and NO_3^-) in the synthesis process. The chemical reaction is complete at $\sim 600/620^\circ\text{C}$ and results in the formation of ZnAl_2O_4 nanoparticles. However, for ZnAl_2O_4

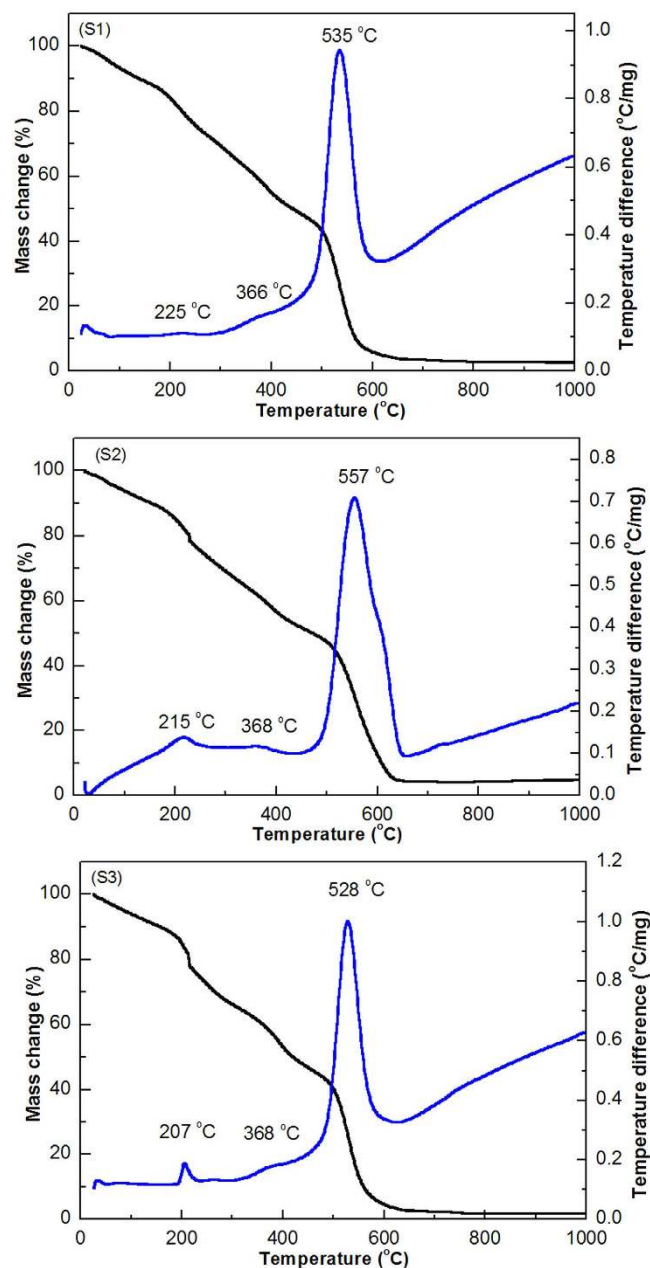


Figure 3. TG/DTA curves of ZnAl_2O_4 xerogel prepared from (S1) $\text{Al}_2(\text{SO}_4)_3 \cdot 18\text{H}_2\text{O}$, (S2) $\text{AlCl}_3 \cdot 6\text{H}_2\text{O}$, and (S3) $\text{Al}(\text{NO}_3)_3 \cdot 9\text{H}_2\text{O}$.

nanoparticles prepared from $\text{Al}_2(\text{SO}_4)_3 \cdot 18\text{H}_2\text{O}$, a higher heat treatment temperature is usually needed to improve the phase purity.

To confirm whether the formation of ZnAl_2O_4 nanoparticles prepared from $\text{Al}_2(\text{SO}_4)_3 \cdot 18\text{H}_2\text{O}$ needed a higher heat treatment temperature, FT-IR measurements were carried out using a Bruker IFS 66 v/S spectrometer. The FT-IR spectra of the ZnAl_2O_4 xerogel prepared from $\text{Al}_2(\text{SO}_4)_3 \cdot 18\text{H}_2\text{O}$ and sintered at different temperatures are presented in Fig. 4. Here it can be seen that the S=O asymmetric stretching vibration (1186 cm^{-1}) and S-O symmetric stretching vibration (1117 cm^{-1}) peak intensities decrease with the increase of sintering temperature. This result indicates that the SO_4^{2-} anion coordinates to Zn and Al cations and forms a bridged bidentate structure^{23,29,30}.

In the case of the sample obtained by sintering the xerogel at 900°C , all of the organic peaks disappear except for the H-O-H peak (1633 cm^{-1}). These results indicate that the effects of aluminum salts and sintering temperature on the phase purity of ZnAl_2O_4 cannot be neglected. Based on the subtle information gathered from the XRD and FT-IR results, the relevant reactions can be described as follows:

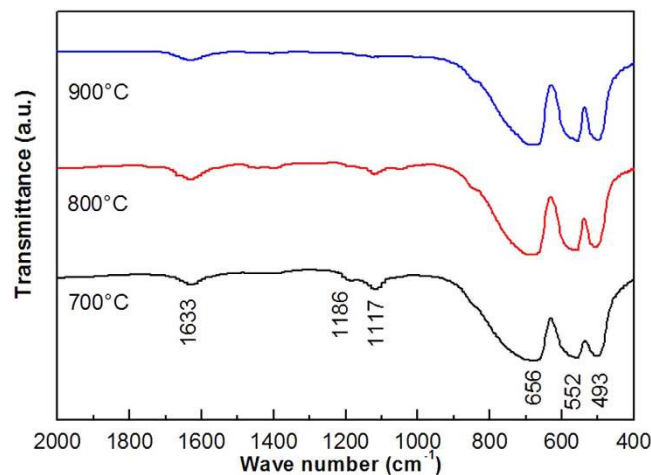
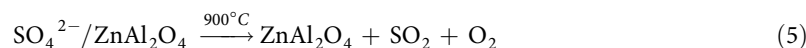
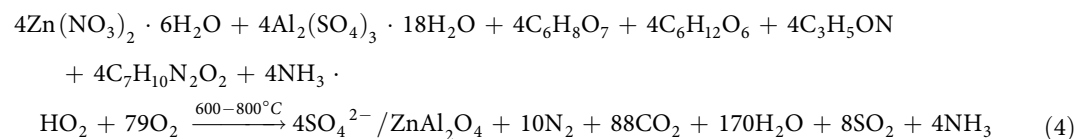


Figure 4. FT-IR spectrum of ZnAl_2O_4 xerogel prepared from $\text{Al}_2(\text{SO}_4)_3 \cdot 18\text{H}_2\text{O}$ and sintered at 700, 800, and 900 °C.



The results indicate that the reaction (1) cannot occur at 600 °C, and that a higher sintering temperature is needed for the formation of pure ZnAl_2O_4 nanoparticles.

In order to investigate the effects of different aluminum salts on the formation of ZnAl_2O_4 , including the particle size and surface morphology, SEM and TEM images were collected of the ZnAl_2O_4 samples prepared using different aluminum salts and sintered at 700 °C, and are shown in Fig. 5 and Fig. 6. The SEM images of the ZnAl_2O_4 samples reveal that the particles are almost spherical in shape and have a narrow particle size distribution (Fig. 5(S1–S3)). When $\text{AlCl}_3 \cdot 6\text{H}_2\text{O}$ is added into the ZnAl_2O_4 precursor, large particles form, however, if $\text{Al}_2(\text{SO}_4)_3 \cdot 18\text{H}_2\text{O}$ is added into the precursor, small particles with little adhesion are observed, as shown in Fig. 5(S1–S2).

Figure 6 shows (S1–S3) TEM image, (SH1–SH3) HRTEM image, and (SP1–SP3) the particle size distribution of ZnAl_2O_4 nanoparticles prepared from (S1) $\text{Al}_2(\text{SO}_4)_3 \cdot 18\text{H}_2\text{O}$, (S2) $\text{AlCl}_3 \cdot 6\text{H}_2\text{O}$, and $\text{Al}(\text{NO}_3)_3 \cdot 9\text{H}_2\text{O}$. The ZnAl_2O_4 nanoparticles are spherical in shape with a narrow particle size distribution, as shown in Fig. 6(S1–S3). The corresponding particle size distribution patterns are given in the Fig. 6 (SP1–SP3). The average particle sizes of samples S1, S2, and S3 are around 12, 18, and 24 nm, respectively. TEM results show that the particle size variation tendencies for samples S1, S2, and S3 are consistent with those calculated from XRD patterns (Fig. 1). In addition, the BET surface area of the sample decreases with the increase of particle size as shown in Table 1. Compared with sample S2, the average particle size and BET surface area of sample S1 is significantly reduced, an effect which may be due to the SO_4^{2-} anion forming a bridged bidentate structure³¹. Fig. 6(S2) inset presents the SAED pattern taken from a portion of the ZnAl_2O_4 nanoparticles shown in Fig. 6(S2). The associated electron diffraction pattern is consistent with that of pure ZnAl_2O_4 crystals of a spinel structure, indexed as shown in Fig. 1(a). The SAED pattern revealed that the ZnAl_2O_4 nanoparticles possess interplanar spacings of 2.8235, 2.4156, 2.0205, 1.6328, 1.5531, and 1.4203 Å corresponding to the (220), (311), (400), (422), (511), and (440) planes, respectively.

Figure 6 (SH1)–(SH3) shows the HRTEM image of ZnAl_2O_4 nanoparticles prepared from (S1) $\text{Al}_2(\text{SO}_4)_3 \cdot 18\text{H}_2\text{O}$, (S2) $\text{AlCl}_3 \cdot 6\text{H}_2\text{O}$, and (S3) $\text{Al}(\text{NO}_3)_3 \cdot 9\text{H}_2\text{O}$. For these samples, the lattice planes of ZnAl_2O_4 nanoparticles were (111) with a lattice space of 4.6687 Å, (220) with a lattice space of 2.8437 Å, (222) with a lattice space of 2.3345 Å, (400) with a lattice space of 2.0210 Å, (331) with a lattice space of 1.8550 Å, and (440) with a lattice space of 1.4356 Å. It has been noted that (111), (220), (222), (400), (331) and (440) planes can be attributed to spinel ZnAl_2O_4 structure corresponding to JCPDS card No. 05–0669.

Figure 7(a) shows the UV-Vis diffuse reflectance spectra of ZnAl_2O_4 samples prepared from (S1) $\text{Al}_2(\text{SO}_4)_3 \cdot 18\text{H}_2\text{O}$, (S2) $\text{AlCl}_3 \cdot 6\text{H}_2\text{O}$, and (S3) $\text{Al}(\text{NO}_3)_3 \cdot 9\text{H}_2\text{O}$. Considering that ZnAl_2O_4 is a direct band-gap semiconductor³², the E_g of the ZnAl_2O_4 samples can be estimated from plots of $(\alpha h\nu)^2$ versus $h\nu$

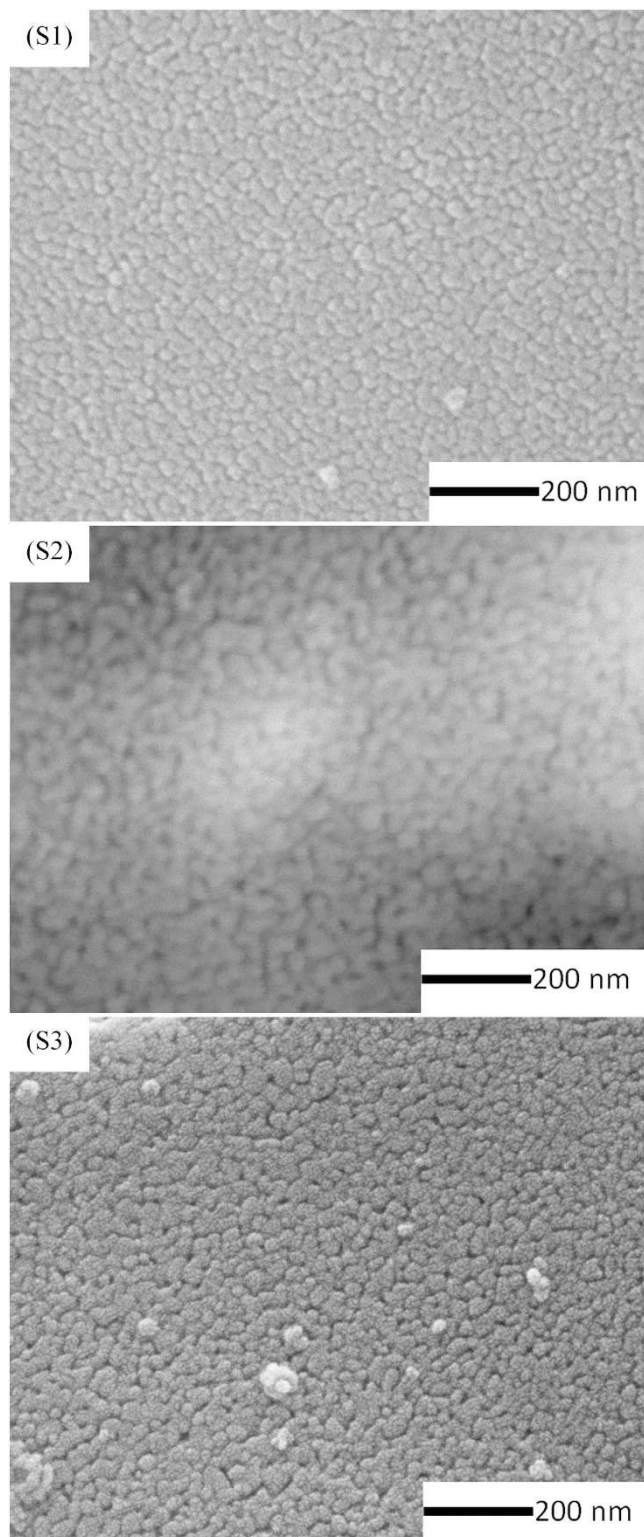


Figure 5. SEM images and particle size distribution of ZnAl_2O_4 xerogel prepared from (S1) $\text{Al}_2(\text{SO}_4)_3 \cdot 18\text{H}_2\text{O}$, (S2) $\text{AlCl}_3 \cdot 6\text{H}_2\text{O}$, and (S3) $\text{Al}(\text{NO}_3)_3 \cdot 9\text{H}_2\text{O}$ and sintered at 700°C .

using the Tauc relation³³. This is shown in Fig. 7(b), where h is the Planck constant, α is the Kubelka–Munk (K–M) absorption coefficient, and ν is the frequency. The linear portions of the plots are extrapolated to the $h\nu$ axis to give the values of E_g . The calculated E_g values of samples S1, S2, and S3 are 3.98 ± 0.01 , 3.92 ± 0.01 and 3.22 ± 0.01 eV, respectively. Generally, the E_g values of nano-sized semiconductors increase with a decrease in particle size. In this case, the observed phenomenon is consistent with what has been previously reported.

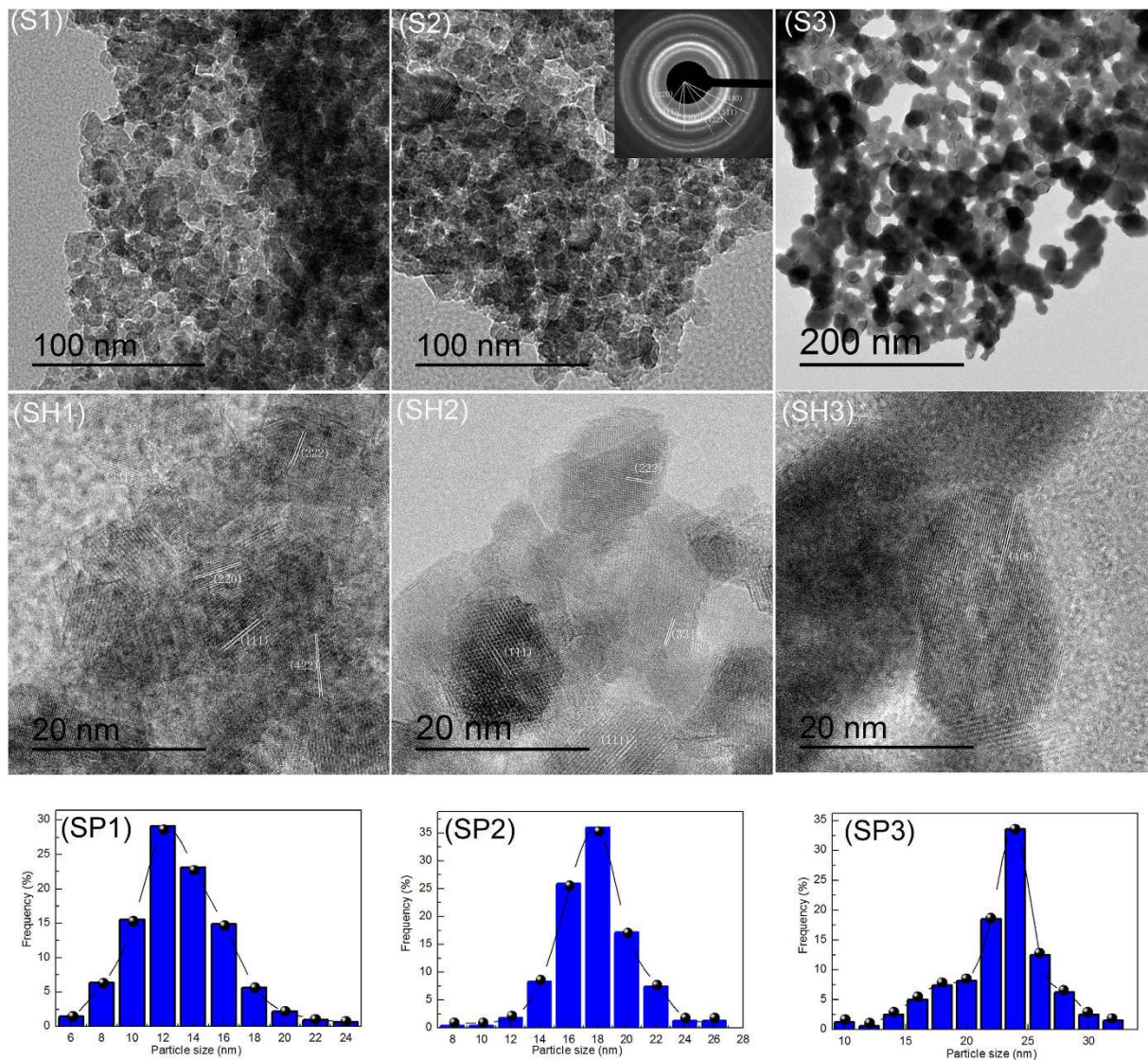


Figure 6. (S1–S3) TEM image, (SH1–SH3) HRTEM image, and (SP1–SP3) Particle size distribution of ZnAl_2O_4 nanoparticles prepared from (S1) $\text{Al}_2(\text{SO}_4)_3 \cdot 18\text{H}_2\text{O}$, (S2) $\text{AlCl}_3 \cdot 6\text{H}_2\text{O}$, and (S3) $\text{Al}(\text{NO}_3)_3 \cdot 9\text{H}_2\text{O}$ and sintered at 700°C . The inset presents the SAED pattern taken from a portion of the ZnAl_2O_4 nanoparticles shown in Fig. 6(S2).

Sample	Crystallite size (nm)	Particle size (nm)	Eg (eV)	BET specific surface area (m^2/g)
S1	13	12	3.98	40.13
S2	16	18	3.92	27.75
S3	24	24	3.22	19.38

Table 1. Crystallite size, particle size, Eg and BET specific surface area of samples S1, S2 and S3.

Figure 8(a) show the fluorescence spectra of ZnAl_2O_4 samples prepared from (S1) $\text{Al}_2(\text{SO}_4)_3 \cdot 18\text{H}_2\text{O}$, (S2) $\text{AlCl}_3 \cdot 6\text{H}_2\text{O}$, and (S3) $\text{Al}(\text{NO}_3)_3 \cdot 9\text{H}_2\text{O}$ and sintered at 700°C . The fluorescence spectra with a wavelength range of $385 \sim 445 \text{ nm}$ for all samples are presented after excitation with light, $\lambda_{\text{exc}} = 325 \text{ nm}$. The fluorescence spectrum of the ZnAl_2O_4 sample is wide and can be resolved using three Gaussian peaks at 400, 410, and 445 nm (Fig. 8b). The three emission peaks at 400, 410, and 445 nm can be ascribed to intra band gap defects such as oxygen vacancies³⁴. It has been noted that there is an obvious increase in the fluorescence intensity of the peak located at 400 nm when the Eg value decreases (see Fig. 8(a) inset).

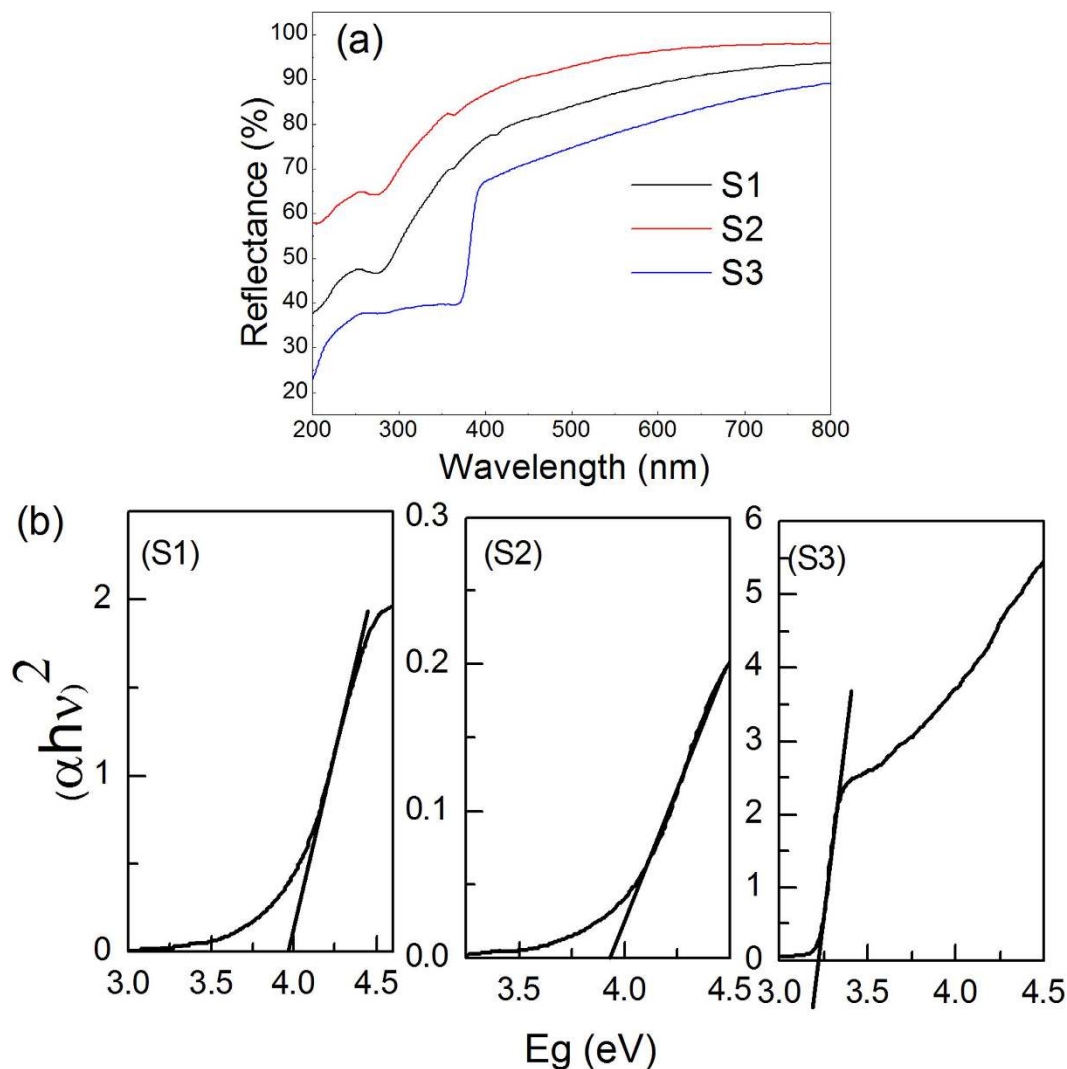


Figure 7. (a) UV-Vis diffuse reflectance spectra and (b) E_g values of ZnAl_2O_4 samples prepared from (S1) $\text{Al}_2(\text{SO}_4)_3 \cdot 18\text{H}_2\text{O}$, (S2) $\text{AlCl}_3 \cdot 6\text{H}_2\text{O}$, and (S3) $\text{Al}(\text{NO}_3)_3 \cdot 9\text{H}_2\text{O}$ and sintered at 700°C .

Compared with the ZnAl_2O_4 nanoparticles prepared from $\text{Al}_2(\text{SO}_4)_3 \cdot 18\text{H}_2\text{O}$, the ZnAl_2O_4 nanoparticles obtained from $\text{AlCl}_3 \cdot 6\text{H}_2\text{O}$ have a smaller E_g value, however, their fluorescence intensity is also smaller. Therefore, in this case we cannot simply attribute the differences in the fluorescence intensity for the three ZnAl_2O_4 samples only to the differences in their E_g values. The difference in the fluorescence intensity of the two ZnAl_2O_4 samples may also be related to the different phase purities of ZnAl_2O_4 samples prepared from (S1) $\text{Al}_2(\text{SO}_4)_3 \cdot 18\text{H}_2\text{O}$ and (S2) $\text{AlCl}_3 \cdot 6\text{H}_2\text{O}$. In the case of the ZnAl_2O_4 sample prepared from $\text{Al}_2(\text{SO}_4)_3 \cdot 18\text{H}_2\text{O}$, traces of the S=O and S-O are visible in the FT-IR spectrum after sintering at 700°C .

Discussion

In order to understand the fluorescence mechanism of the prepared ZnAl_2O_4 samples, it is necessary to propose a schematic band diagram to illustrate the process of excitation and emission for the system. Figure 9 shows a schematic band diagram for the fluorescence mechanism of ZnAl_2O_4 samples obtained from (S1) $\text{Al}_2(\text{SO}_4)_3 \cdot 18\text{H}_2\text{O}$, (S2) $\text{AlCl}_3 \cdot 6\text{H}_2\text{O}$, and (S3) $\text{Al}(\text{NO}_3)_3 \cdot 9\text{H}_2\text{O}$. It is known that Al^{3+} $2p$ orbitals and s orbitals located at the upper part of the Al^{3+} $2p$ orbitals and s orbitals make up the major conduction band (CB) edge of ZnAl_2O_4 , and the hybridization band composed of O^{2-} $2p$ and Zn^{2+} $3d$ orbitals makes up the upper valence band (VB)³⁵. When the E_g value $> \lambda_{exc}$ (3.82 eV vs. 325 nm) it can be seen that one electron transition occurs from VB onto the intra band gap defects (IBGD) energy level (Fig. 9(S1) and (S2)). After that, the electron will be driven by continued transition from IBDG to CB. Then, the electron on the CB drops down to the low energy level through loss of energy by vibration relaxation (VR). Finally, the electron on the low energy level undergoes a radiative recombination with a hole in the valence band, accompanied by three blue-light emissions. For sample S1, the impurity (SO_4^{2-}) plays a crucial role to

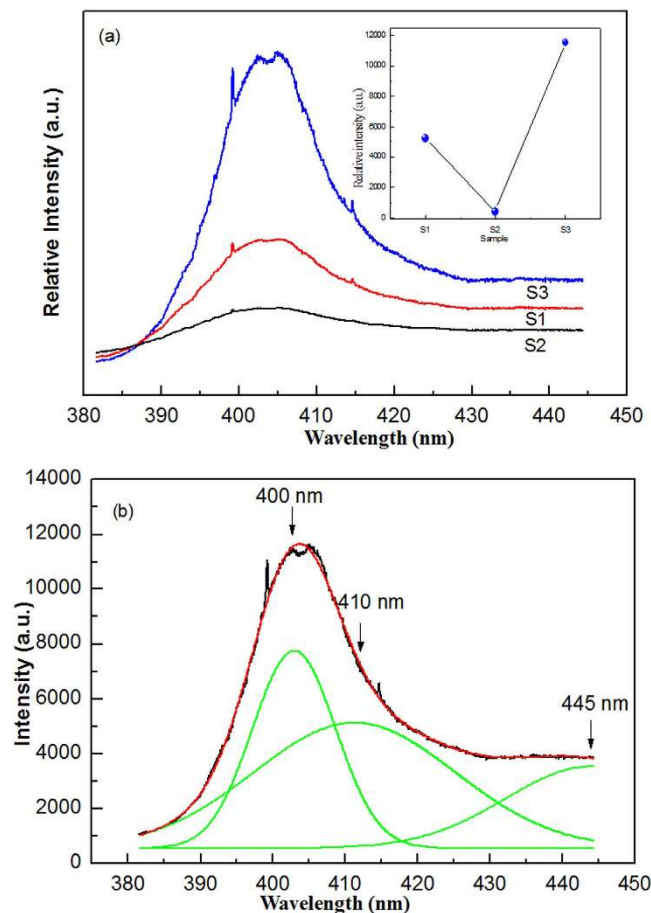


Figure 8. Fluorescence spectra of ZnAl_2O_4 samples prepared from (S1) $\text{Al}_2(\text{SO}_4)_3 \cdot 18\text{H}_2\text{O}$, (S2) $\text{AlCl}_3 \cdot 6\text{H}_2\text{O}$, and (S3) $\text{Al}(\text{NO}_3)_3 \cdot 9\text{H}_2\text{O}$ and sintered at 700°C .

promote the electron transition from IL (impurity level) to CB and improve the fluorescence properties. When $E_g < \lambda_{exc}$, one electron transition occurs from the VB to the high energy level (Fig. 9(S3)). Then, the electron on the high energy level drops down to the CB by internal conversion. At the same time, the electron on the CB by VR drops down to the low energy level with an accompanying loss of energy. Finally, the electron on the low energy level undergoes a radiative recombination with a hole in the valence band, accompanied by a series of blue-light emissions.

Figure 10 shows the Commission International De l'Eclairage (CIE) diagram of a ZnAl_2O_4 phosphor under 325 nm laser excitations. The CIE color coordinates (x, y) of the ZnAl_2O_4 phosphor was calculated using the fluorescence spectra. A typical CIE color coordinate of a ZnAl_2O_4 phosphor was found to be x, y equals 0.1729, 0.0048 respectively under 325 nm laser excitations.

According to equation (7)³⁶, the fluorescence quantum efficiency of the ZnAl_2O_4 phosphor can be calculated from the experimental data.

$$QE_s = QE_{s-s} \times \frac{\int I_s}{\int I_{s-s}} \times \frac{A_{s-s}}{A_s} \quad (7)$$

Where QE_s and QE_{s-s} are the fluorescence quantum efficiencies of the prepared sample and standard sample, respectively, under an excitation wavelength of 325 nm. $\int I_s$ and $\int I_{s-s}$ are the integrated emission intensities of the prepared sample and standard sample under an excitation wavelength of 325 nm. A_s and A_{s-s} are the absorbance of the prepared sample and standard sample under an excitation wavelength of 325 nm. The standard sample is 5-sulfosalicylic acid, which has a quantum efficiency of about 58% under an excitation wavelength of 325 nm. The fluorescence quantum efficiencies of samples S1, S2, and S3 were calculated to be 6.38%, 4.24%, and 10.11%, respectively. Observations made during these experiments show that the spinel ZnAl_2O_4 phosphor could be useful for blue light-emitting materials.

In summary, ZnAl_2O_4 nanoparticles with different particle sizes were prepared using a modified polyacrylamide gel route from different aluminum salt starting materials: $\text{Al}_2(\text{SO}_4)_3 \cdot 18\text{H}_2\text{O}$, $\text{AlCl}_3 \cdot 6\text{H}_2\text{O}$, and $\text{Al}(\text{NO}_3)_3 \cdot 9\text{H}_2\text{O}$. The type of aluminum salt used can markedly influence the phase purity, particle

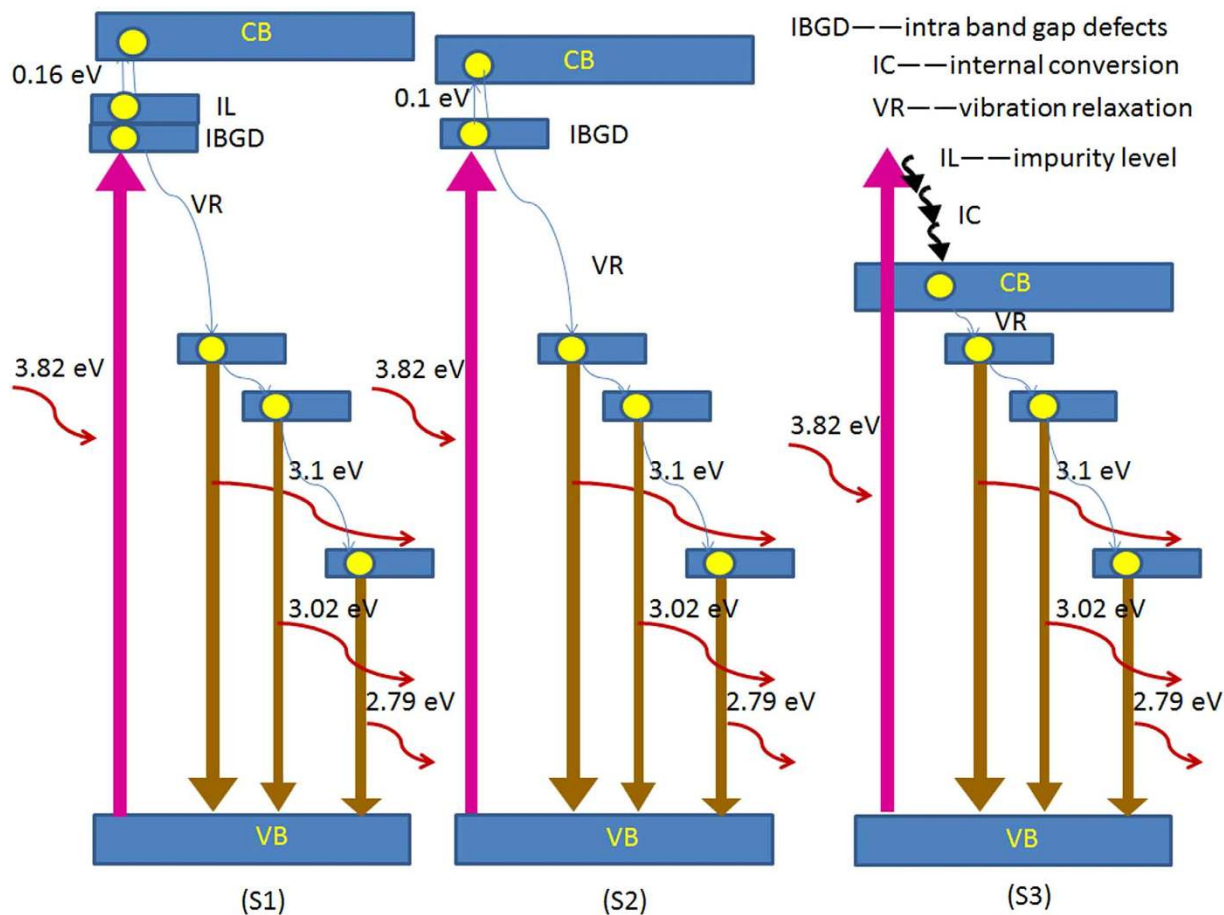


Figure 9. Fluorescence mechanism of $ZnAl_2O_4$ samples prepared from (S1) $Al_2(SO_4)_3 \cdot 18H_2O$, (S2) $AlCl_3 \cdot 6H_2O$, and (S3) $Al(NO_3)_3 \cdot 9H_2O$.

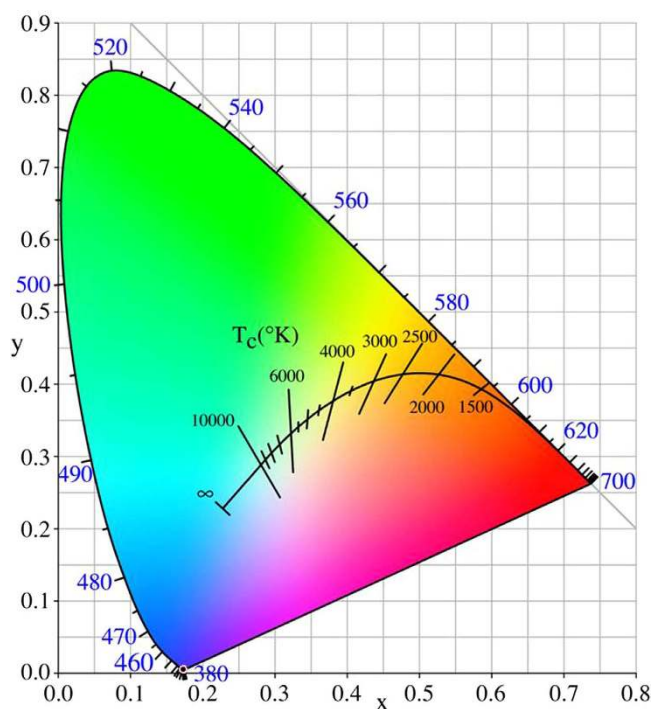


Figure 10. CIE diagram of $ZnAl_2O_4$ phosphor under 325 nm laser excitations.

Sample	Al ₂ (SO ₄) ₃ ·18H ₂ O	AlCl ₃ ·6H ₂ O	Al(NO ₃) ₃ ·9H ₂ O	Zn(NO ₃) ₂ ·6H ₂ O	citric acid	glucose	acrylamide	Bis-acrylamide
S1	6.6644g	/	/	1.4875 g	4.7282g	20 g	9.5958g	1.9192g
S2	/	2.4143g	/	1.4875 g	4.7282g	20 g	9.5958g	1.9192g
S3	/	/	3.7513g	1.4875 g	4.7282g	20 g	9.5958g	1.9192g

Table 2. Starting compositions of samples S1, S2 and S3.

size, and optical and fluorescence properties of the final product. Under 325 nm excitation, samples of ZnAl₂O₄ phosphor show blue emissions and the CIE colour coordinate was found to be (0.1729, 0.0048). The fluorescence mechanisms of the ZnAl₂O₄ phosphor have been discussed based on the experimental results. The fluorescence experiments revealed that the as-prepared ZnAl₂O₄ phosphor exhibits interesting abilities for application in blue light-emitting materials. Interestingly, similar preparation methods may be employed for the synthesis of other metal oxides nanoparticles, including fluorescence materials, multiferroic materials, oxide thermoelectric materials, photocatalytic materials, solid oxide fuel cell materials, and high-temperature superconducting materials.

Methods

Materials. Zn(NO₃)₂·6H₂O, AlCl₃·6H₂O, Al₂(SO₄)₃·18H₂O, and Al(NO₃)₃·9H₂O were purchased from DaMao Chem. Ltd., Tianjing. Citric acid (C₆H₈O₇, AR), glucose (C₆H₁₂O₆·H₂O, 99%), acrylamide (C₃H₅NO, AR), and N, N'-methylene-bisacrylamide (C₇H₁₀N₂O₂, 99%) were purchased from Kemiou Chem. Ltd., Tianjing and used without further purification.

Synthesis. A certain stoichiometric amounts of Zn(NO₃)₂·6H₂O and different aluminum salts (Al₂(SO₄)₃·18H₂O, AlCl₃·6H₂O, and Al(NO₃)₃·9H₂O are labeled sample S1, S2 and S3, respectively) were dissolved in the deionized water to obtain a final solution of 0.015 mol/L with the total cations. Starting compositions of samples S1, S2 and S3 are given in Table 2. After the solution was transparent, a stoichiometric amount of chelating agent (citric acid) was added into the solution in the mole ratio 1.5:1 with respect to the total cations (Zn²⁺ and Al³⁺) to complex the cations. After that, 20 g glucose was dissolved into the solution. Finally, the acrylamide and N, N'-methylene-bisacrylamide monomers were added into the solution. The resultant solution was heated to 90 °C on a hot plate to initiate the polymerization reaction, and a few minutes later a polyacrylamide gel was formed. The gel was dried at 120 °C for 24 h in a thermostat drier. The obtained xerogel precursor was ground into powder and some powder was sintered at 600, 700, 800, and 900 °C for 5 h in air to prepare the objective products.

Sample characterization. The ZnAl₂O₄ xerogel precursor sintered at 600 and 700 °C were analyzed by X-ray diffractometer (DX-2700) with Cu Kα radiation. Fourier transform infrared (FTIR) spectra in the range 400–2000 cm⁻¹ were recorded using a Bruker IFS 66 v/S spectrometer. Thermogravimetric (TG) and differential thermal analysis (DTA) analyses were performed in a SDT Q600 (TA instruments, Inc. USA) simultaneous thermal analyzer at a heating rate of 10 °C/min. The surface morphology of the synthesized ZnAl₂O₄ sample was characterized by scanning electron microscopy (SEM) and transmission electron microscopy (TEM). The surface area of the samples were characterized by a 3H-2000BET-M instrument. The absorption spectra of the samples were examined on a Shimadzu UV-2500 UV-Visible spectrophotometer. The fluorescence spectra were collected at room temperature in a confocal Raman system using a He-Cd laser (325 nm, RGB laser system, NovaPro 30 mW, Germany).

References

- Duan, X. L., Yuan, D. R. & Yu, F. P. Cation distribution in Co-doped ZnAl₂O₄ nanoparticles studied by X-ray photoelectron spectroscopy and ²⁷Al solid-state NMR spectroscopy. *Inorg. Chem.* **50**, 5460–5467 (2011).
- Ianos, R., Borcǎnescu, S. & Lazaǎu, R. Large surface area ZnAl₂O₄ powders prepared by a modified combustion technique. *Chem. Eng. J.* **240**, 260–263 (2014).
- Foletto, E. L. *et al.* Synthesis of ZnAl₂O₄ nanoparticles by different routes and the effect of its pore size on the photocatalytic process. *Micropor. Mesopor. Mat.* **163**, 29–33 (2012).
- Li, X. Y., Zhu, Z. R., Zhao, Q. D. & Wang, L. Z. Photocatalytic degradation of gaseous toluene over ZnAl₂O₄ prepared by different methods: A comparative study. *J. Hazard. Mater.* **186**, 208–2096 (2011).
- Peng, C. *et al.* Fabrication and luminescence properties of one-dimensional ZnAl₂O₄ and ZnAl₂O₄: A³⁺ (A = Cr, Eu, Tb) microfibers by electrospinning method. *Mater. Res. Bull.* **47**, 3592–3599 (2012).
- Cheng, B. C., Ouyang, Z. Y., Tian, B. X., Xiao, Y. H. & Lei, S. J. Porous ZnAl₂O₄ spinel nanorods: high sensitivity humidity sensors. *Ceram. Int.* **39**, 7379–7386 (2013).
- Zhu, Z. R. *et al.* Photocatalytic performances and activities of ZnAl₂O₄ nanorods loaded with Ag towards toluene. *Chem. Eng. J.* **203**, 43–51 (2012).
- Yang, Y. *et al.* Hierarchical three-dimensional ZnO and their shape-preserving transformation into hollow ZnAl₂O₄ nanostructures. *Chem. Mater.* **20**, 3487–3494 (2008).
- Zou, L., Li, F., Xiang, X., Evans, D. G. & Duan, X. Self-generated template pathway to high-surface-area zinc aluminate spinel with mesopore network from a single-source inorganic precursor. *Chem. Mater.* **18**, 5852–585 (2006).
- Van der Laag, N.J., Snel, M.D., Magusin, P. C. M. M. & De With, G. Structural, elastic, thermophysical and dielectric properties of zinc aluminate (ZnAl₂O₄). *J. Eur. Ceram. Soc.* **24**, 2417–2424 (2004).

11. Ianos, R., Lazău, R., Lazău, I. & Păcurariu, C. Chemical oxidation of residual carbon from ZnAl₂O₄ powders prepared by combustion synthesis. *J. Eur. Ceram. Soc.* **32**, 1605–1611 (2012).
12. Wei, X. & Chen, D. Synthesis and characterization of nanosized zinc aluminate spinel by sol-gel technique. *Mater. Lett.* **60**, 823–827 (2006).
13. Gama, L. *et al.* Synthesis and characterization of the NiAl₂O₄, CoAl₂O₄ and ZnAl₂O₄ spinels by the polymeric precursors method. *J. Alloys Comp.* **483**, 453–455 (2009).
14. Fan, G. L., Wang, J. & Li, F. Synthesis of high-surface-area micro/mesoporous ZnAl₂O₄ catalyst support and application in selective hydrogenation of o-chloronitrobenzene. *Catal. Commun.* **15**, 113–117 (2011).
15. Zawadzki, M., Staszak, W., López-Suárez, F.E., Illán-Gómez, M. J. & Bueno-López, A. Preparation, characterisation and catalytic performance for soot oxidation of copper-containing ZnAl₂O₄ spinels. *Appl. Catal. A: Gen.* **371**, 92–98 (2009).
16. Yu, Z.Q., Li, C. & Zhang, N. Size dependence of the luminescence spectra of nanocrystal alumina. *J. Lumin.* **99**, 29–34 (2002).
17. Wang, S. F., Lv, H. B., Zhou, X. S., Fu, Y. Q. & Zu, X. T. Magnetic nanocomposites through polyacrylamide gel route. *Nanosci. Nanotech. Lett.* **6**, 758–771 (2014).
18. Theophil Anand, G., John Kennedy, L., Aruldoss, U. & Judith Vijaya, J. Structural, optical and magnetic properties of Zn_{1-x}Mn_xAl₂O₄ (0 ≤ x ≤ 5) spinel nanostructures by one-pot microwave combustion technique. *J. Mol. Struct.* **1084**, 244–253 (2015).
19. Ge, D. L., Fan, Y. J., Qi, C.L. & Sun, Z. X. Facile synthesis of highly thermostable mesoporous ZnAl₂O₄ with adjustable pore size. *J. Mater. Chem. A* **1**, 1651–1658 (2013).
20. Silva, A. A. D., De Souza Goncalves, A. & Davolos, M. R. Characterization of nanosized ZnAl₂O₄ spinel synthesized by the sol-gel method. *J. Sol-Gel Sci. Technol.* **49**, 101–105 (2009).
21. Huang, I. B. *et al.* Preparation and luminescence of green-emitting ZnAl₂O₄:Mn²⁺ phosphor thin films. *Thin Solid Films* **570**, 451–456 (2014).
22. Theophil Anand, G., John Kennedy, L., Judith Vijaya, J., Kaviyaran, K. & Sukumar, M. Structural, optical and magnetic characterization of Zn_{1-x}Ni_xAl₂O₄ (0 ≤ x ≤ 5) spinel nanostructures synthesized by microwave combustion technique. *Ceram. Int.* **41**, 603–615 (2015).
23. Yamaguchi, T., Jin, T. & Tanabe, K. Structure of acid sites on sulfur-promoted iron oxide. *J. Phys. Chem.* **90**, 3148–3152 (1986).
24. Wang J. X. *et al.* Synthesis and characterization of S₂O₈²⁻/ZnFe_xAl_{2-x}O₄ solid acid catalysts for the esterification of acetic acid with n-butanol. *Catal. Commun.* **62**, 29–33 (2015).
25. Zhang, Y., Zhao, C.Y., Liang, H. & Liu, Y. Macroporous monolithic Pt/α-Al₂O₃ and K-Pt/α-Al₂O₃ catalysts used for preferential oxidation of CO. *Catal. Lett.* **127**, 339–347 (2009).
26. Zhang, Y., Liang, H., Zhao, C. Y. & Liu, Y. Macroporous alumina monoliths prepared by filling polymer foams with alumina hydrosols. *J. Mater. Sci.* **44**, 931–938 (2009).
27. Xian, T. *et al.* Preparation of high-quality BiFeO₃ nanopowders via a polyacrylamide gel route. *J. Alloy. Comp.* **480**, 889–892 (2009).
28. Wu, S. Q., Liu, Y. Y., He, L. N. & Wang, F. P. Preparation of β-spodumene-based glass-ceramic powders by polyacrylamide gel process. *Mater. Lett.* **58**, 2772–2775 (2004).
29. Eskenazi, R., Raskovan, J. & Levitus, R. Sulphato complexes of palladium (II). *J. Inorg. Nucl. Chem.* **28**, 521–526 (1966).
30. Schoonheydt, R. A. & Lunsford, J. H. Infrared spectroscopic investigation of the adsorption and reactions of SO₂ on MgO. *J. Catal.* **26**, 261–271 (1972).
31. Coma, A. Inorganic solid acids and their use in acid-catalyzed hydrocarbon reactions. *Chem. Rev.* **95**, 559–614 (1995).
32. Dixit, H. *et al.* First-principles study of possible shallow donors in ZnAl₂O₄ spinel. *Phys. Rev. B* **87**, 174101 (2013).
33. Ragupathi, C., Judith Vijaya, J., Manikandan, A. & John Kennedy, L. Phytosynthesis of nanoscale ZnAl₂O₄ by using sesamum (*Sesamum indicum* L.) optical and catalytic properties. *J. Nanosci. Nanotechnol.* **13**, 8298–8306 (2013).
34. Ragupathi, C., Kennedy, L. J. & Vijaya, J. J. A new approach: Synthesis, characterization and optical studies of nano-zinc aluminate. *Adv. Powder Technol.* **25**, 267–273 (2014).
35. Khenata, R. *et al.* Full-potential calculations of structural, elastic and electronic properties of MgAl₂O₄ and ZnAl₂O₄ compounds. *Phys. Lett. A* **344**, 271–279 (2005).
36. Demasa, J. N. & Crosby, G. A. The measurement of photoluminescence quantum yields. A review. *J. Phys. Chem.* **75**, 991–1024 (1971).

Acknowledgements

This work was supported by the NSAF joint Foundation of China (U1330103) and by Outstanding Doctoral Student Support Plan (A1098524023901001074).

Author Contributions

S.W. and G.S. contributed to the preparation and characterization of the nanoparticles. L.L. measured the fluorescence spectra. S.W., G.S., L.F. and X.X. analyzed data from experiments and wrote the main manuscript. X.Z. led the project.

Additional Information

Competing financial interests: The authors declare no competing financial interests.

How to cite this article: Wang, S.-F. *et al.* A comparative study of ZnAl₂O₄ nanoparticles synthesized from different aluminum salts for use as fluorescence materials. *Sci. Rep.* **5**, 12849; doi: 10.1038/srep12849 (2015).



This work is licensed under a Creative Commons Attribution 4.0 International License. The images or other third party material in this article are included in the article's Creative Commons license, unless indicated otherwise in the credit line; if the material is not included under the Creative Commons license, users will need to obtain permission from the license holder to reproduce the material. To view a copy of this license, visit <http://creativecommons.org/licenses/by/4.0/>